

---

# UNSUPERVISED DISCOVERY OF INTERMEDIATE PHASE ORDER IN THE FRUSTRATED $J_1$ - $J_2$ HEISENBERG MODEL VIA PROMETHEUS FRAMEWORK

---

PREPRINT

Brandon Yee,<sup>1</sup> Wilson Collins,<sup>1</sup> Maximilian Rutkowski,<sup>1</sup><sup>1</sup>Physics Lab, Yee Collins Research Group

{b.yee, w.collins, r.rutkowski}@ycrg-labs.org

**ABSTRACT**

The spin-1/2  $J_1$ - $J_2$  Heisenberg model on the square lattice exhibits a debated intermediate phase between Néel antiferromagnetic and stripe ordered regimes, with competing theories proposing plaquette valence bond, nematic, and quantum spin liquid ground states. We apply the Prometheus variational autoencoder framework—previously validated on classical (2D, 3D Ising) and quantum (disordered transverse field Ising) phase transitions—to systematically explore the  $J_1$ - $J_2$  phase diagram via unsupervised analysis of exact diagonalization ground states for a  $4 \times 4$  lattice. Through dense parameter scans of  $J_2/J_1 \in [0.3, 0.7]$  with step size 0.01 and comprehensive latent space analysis, we investigate the nature of the intermediate regime using unsupervised order parameter discovery and critical point detection via multiple independent methods. This work demonstrates the application of rigorously validated machine learning methods to open questions in frustrated quantum magnetism, where traditional order parameter identification is challenged by competing interactions and limited accessible system sizes.

**Keywords** Quantum phase transitions · Frustrated magnetism · J1-J2 Heisenberg model · Variational autoencoders · Unsupervised learning · Order parameter discovery

**1 Introduction****1.1 The  $J_1$ - $J_2$  Heisenberg Problem**

The spin-1/2  $J_1$ - $J_2$  Heisenberg model on the square lattice stands as one of the paradigmatic models in frustrated quantum magnetism, exhibiting rich physics arising from the competition between nearest-neighbor ( $J_1$ ) and next-nearest-neighbor ( $J_2$ ) antiferromagnetic interactions. The Hamiltonian is defined as

$$H = J_1 \sum_{\langle i,j \rangle} \vec{S}_i \cdot \vec{S}_j + J_2 \sum_{\langle\langle i,k \rangle\rangle} \vec{S}_i \cdot \vec{S}_k, \quad (1)$$

where  $\vec{S}_i$  are spin-1/2 operators,  $J_1, J_2 > 0$  are antiferromagnetic coupling constants, and the sums run over nearest-neighbor and next-nearest-neighbor pairs respectively.

For small frustration ratio  $J_2/J_1 \ll 1$ , the ground state exhibits Néel antiferromagnetic order with staggered magnetization  $\vec{m}_s = N^{-1} \sum_i (-1)^{i_x+i_y} \langle \vec{S}_i \rangle$  [1, 2]. For large frustration  $J_2/J_1 \gg 1$ , the system develops stripe (columnar) order where spins align ferromagnetically along one lattice direction and antiferromagnetically along the other [3]. The exact Majumdar-Ghosh point at  $J_2/J_1 = 0.5$  in the one-dimensional variant admits an exact dimer ground state [1], but no such exact solution exists for the two-dimensional square lattice.

The intermediate regime  $J_2/J_1 \sim 0.4$ – $0.6$  has been the subject of intense theoretical and numerical investigation for over three decades, with no definitive consensus on the nature of the ground state. Competing proposals include:

- **Plaquette valence bond solid (VBS):** A state breaking lattice rotation symmetry with enhanced four-spin plaquette correlations [4, 5].
- **Nematic order:** A state preserving spin-rotation symmetry but breaking lattice symmetries, characterized by directional spin correlations without magnetic order [6].
- **Quantum spin liquid:** An exotic state with no symmetry breaking and fractionalized excitations [7, 8].
- **Direct transition:** A scenario where no intermediate phase exists, with a continuous or weakly first-order transition directly from Néel to stripe order [9, 10].

The resolution of this question carries significance beyond the specific  $J_1$ - $J_2$  model. This system serves as the simplest frustrated quantum magnet on a bipartite lattice and provides insights into:

1. The role of quantum fluctuations in destroying classical magnetic order.
2. Mechanisms for emergent symmetries and exotic ground states in frustrated systems.
3. Connections to high-temperature superconductivity, where similar frustration patterns appear in the parent antiferromagnetic compounds [2].
4. Experimental realizations in organic salts [11], layered cuprates, and cold atom quantum simulators [12].

## 1.2 Computational Challenges

The determination of the intermediate phase structure faces several computational obstacles that have prevented definitive resolution despite decades of study.

**Finite system sizes.** Exact diagonalization (ED) provides numerically exact ground states but is limited by the exponential scaling of the Hilbert space dimension ( $2^N$  for  $N$  spins). State-of-the-art ED calculations on the square lattice are restricted to  $N \lesssim 40$  spins ( $\sim 6 \times 6$  lattice) [13], where finite-size effects can be substantial, particularly in frustrated systems with competing orders.

**Sign problem in quantum Monte Carlo.** While quantum Monte Carlo (QMC) can access larger system sizes, frustrated Heisenberg models typically suffer from the fermion sign problem after Jordan-Wigner transformation, leading to exponentially poor signal-to-noise ratio that limits accessible temperatures and system sizes [13].

**DMRG convergence issues.** Density matrix renormalization group (DMRG) methods can handle larger 2D systems through cylindrical geometries [14, 15], but convergence in frustrated systems is sensitive to initial conditions, bond dimension truncation, and boundary effects. Different initialization schemes can converge to different local minima in the energy landscape [8].

**Unknown order parameters.** Traditional analysis relies on computing correlators for hypothesized order parameters. When the nature of the phase is genuinely unknown—as in the  $J_1$ - $J_2$  intermediate regime—one may not know which observables to measure. Systematically exploring all possible order parameters is computationally prohibitive and may miss exotic order types with no simple local characterization.

**Weak signals in small systems.** Even if the correct order parameter is identified, its magnitude in small systems may be weak due to finite-size effects and quantum fluctuations, making it difficult to distinguish genuine long-range order from finite-size crossover effects [6].

These challenges motivate the development of alternative approaches that can identify phase boundaries and characterize phases without prior knowledge of the order parameter structure.

## 1.3 Machine Learning for Phase Discovery

Machine learning has emerged as a powerful tool for studying phase transitions in condensed matter systems, with approaches broadly classified into supervised and unsupervised methods.

**Supervised approaches** train neural networks on labeled configurations (assigned to known phases) and achieve remarkable classification accuracy. Carrasquilla and Melko [16] demonstrated that convolutional neural networks trained on Monte Carlo configurations of the 2D Ising model can classify phases and locate the critical temperature. Van Nieuwenburg et al. [17] introduced a semi-supervised "learning by confusion" approach that identifies phase boundaries by training classifiers on different parameter regimes and finding regions where they disagree. These methods have been successfully applied to quantum systems [18], topological phases [19], and many-body localization [20].

However, supervised methods face a fundamental limitation: they require labeled training data, which presupposes knowledge of the phase structure—precisely the information one seeks to discover in novel systems. For the  $J_1$ - $J_2$  intermediate regime, we do not know the correct phase labels, making supervised classification circular.

**Unsupervised methods** attempt to discover phase structure from unlabeled data. Wang [21] showed that principal component analysis (PCA) applied to classical Ising configurations yields leading components that correlate with the magnetization order parameter. Wetzel [22] extended this approach using variational autoencoders (VAEs), demonstrating that learned latent representations naturally organize according to phase structure. Rodriguez-Nieva and Scheurer [23] developed interpretable unsupervised learning methods for topological phases, showing that neural networks can discover topological invariants without supervision.

Despite these successes, most unsupervised studies have focused on *validating* the method on systems with known phase diagrams rather than *discovering* genuinely unknown physics. The critical question remains: *Can unsupervised machine learning discover novel quantum phases when applied to open problems where the phase structure is uncertain?*

#### 1.4 The Prometheus Framework

To address this question, we have developed Prometheus, a systematic framework for unsupervised discovery of phase transitions using variational autoencoders, and validated it through a progression of increasingly complex systems.

**2D Ising model validation (Yee et al., 2026a).** We first established the Prometheus methodology on the exactly solvable 2D Ising model [24], where the exact solution provides unambiguous ground truth. Using physics-informed training procedures including symmetry-preserving augmentation and progressive training schedules, we demonstrated automated order parameter discovery correlating with theoretical magnetization, critical temperature detection near the exact Onsager value, and improvement over principal component analysis. This validation on an exactly solvable system established that the VAE latent space naturally captures order parameter physics when trained with appropriate inductive biases, without requiring any labeled phase information or prior knowledge of the magnetization as the relevant degree of freedom.

**Extension to 3D and quantum systems (Yee et al., 2026b).** Having established baseline performance on a solvable system, we extended Prometheus to cases without exact solutions [25], addressing two critical questions: (1) Does the method work when there is no analytical solution to validate against? (2) Can it detect qualitatively different types of critical behavior?

For the 3D classical Ising model, which has no known exact solution, we demonstrated critical temperature detection in agreement with high-precision Monte Carlo benchmarks and critical exponent extraction consistent with the 3D Ising universality class.

For the one-dimensional disordered transverse field Ising model (DTFIM), we demonstrated detection of exotic quantum critical behavior fundamentally different from classical phase transitions, including quantum critical point detection at zero disorder and the first unsupervised detection of activated scaling, successfully distinguishing between conventional power-law scaling (clean system) and activated scaling (disordered system).

The quantum extension introduced several key methodological advances:

1. **Quantum-aware VAE (Q-VAE) architecture:** Modified encoder-decoder to handle complex-valued wavefunctions  $|\psi\rangle = \sum_{\sigma} c_{\sigma} |\sigma\rangle$  with proper normalization  $\langle\psi|\psi\rangle = 1$ .
2. **Fidelity-based loss function:** Replacement of mean squared error with quantum fidelity  $F = |\langle\psi_{\text{in}}|\psi_{\text{recon}}\rangle|^2$  to respect quantum mechanical structure.
3. **Disorder averaging protocols:** Systematic averaging over disorder realizations with bootstrap uncertainty quantification.
4. **Activated scaling detection:** Framework for distinguishing power-law vs. activated critical behavior through latent correlation length analysis.

This systematic progression—exact solution  $\rightarrow$  numerical-only solution  $\rightarrow$  exotic quantum criticality—established Prometheus as a validated tool with demonstrated capability to:

- Discover order parameters without supervision
- Work in the absence of exact analytical solutions
- Detect qualitatively different types of critical phenomena

- Extract quantitative critical properties with controlled uncertainties

Having built confidence through validation on known systems, we are now positioned to apply Prometheus to an open question: *What is the nature of the intermediate phase in the  $J_1$ - $J_2$  Heisenberg model?*

## 1.5 This Work: Discovery Application

In this work, we deploy the validated Prometheus framework to explore the debated intermediate regime of the  $J_1$ - $J_2$  Heisenberg model on the square lattice. Our approach combines:

1. **Comprehensive exact diagonalization:** Ground state calculations for a  $4 \times 4$  lattice across a dense scan of frustration ratios  $J_2/J_1 \in [0.3, 0.7]$  with step size  $\Delta(J_2/J_1) = 0.01$ , yielding 41 ground states.
2. **Quantum-aware variational autoencoder analysis:** Application of the Q-VAE architecture with fidelity-based loss function to learn compressed latent representations of the ground state wavefunctions  $|\psi(J_2/J_1)\rangle$ .
3. **Unsupervised order parameter discovery:** Systematic Pearson correlation analysis between latent dimensions and 11 physical observables (staggered magnetization, stripe order, plaquette order, nematic order, dimer order, structure factors at key wavevectors, energy density, and entanglement entropy) with bootstrap confidence intervals and permutation tests for statistical significance.
4. **Phase boundary detection:** Three independent methods—latent variance peaks, reconstruction error maxima, and fidelity susceptibility—combined via inverse-variance weighted ensemble estimation.
5. **Validation framework:** Automated validation in known Néel and stripe phases, requiring correlation  $|r| \geq 0.7$  with expected order parameters, plus comparison with literature critical point bounds.

The methodology is designed to address the key question while acknowledging the limitations imposed by small accessible system sizes. We do not claim to provide a definitive resolution of the  $J_1$ - $J_2$  phase diagram—which would require system sizes beyond current computational capabilities—but rather to demonstrate that validated unsupervised machine learning can provide meaningful insights into frustrated quantum systems where traditional analysis faces challenges.

Our approach represents a fundamentally different paradigm from previous applications of machine learning to physics: rather than using ML to validate known physics or using physics to validate ML methods, we apply a *rigorously validated ML tool to solve an open physics problem*. The three-paper validation sequence establishes credibility that allows discovery claims to be taken seriously.

## 1.6 Organization

The remainder of this paper is organized as follows. Section 2 describes our computational methodology, including exact diagonalization procedures (Sec. 2.2), the quantum-aware VAE architecture adapted from our previous quantum work (Sec. 2.3), order parameter discovery protocols (Sec. 2.4), and critical point detection methods (Sec. 2.5). Section 3 presents our results, Section 4 discusses their implications in the context of the  $J_1$ - $J_2$  debate, and Section 5 concludes. Detailed technical specifications are provided in the Appendices. All code and data will be made publicly available to enable community validation and extension of this work.

## 2 Methods

### 2.1 The $J_1$ - $J_2$ Heisenberg Model

We study the spin-1/2  $J_1$ - $J_2$  Heisenberg antiferromagnet on a square lattice of linear size  $L = 4$  with periodic boundary conditions, defined by the Hamiltonian of Eq. (1). Throughout this work, we set  $J_1 = 1$  as the energy scale and vary the frustration ratio  $J_2/J_1 \in [0.3, 0.7]$  to explore the transition region.

The Hilbert space dimension for a system of  $N = L \times L = 16$  spins is  $\dim(\mathcal{H}) = 2^{16} = 65,536$ . To make the problem tractable, we exploit conservation of total  $S^z$  (the  $z$ -component of total spin). The  $S_{\text{tot}}^z = 0$  sector, which contains the ground state for antiferromagnetic systems, has dimension

$$\dim(\mathcal{H}_{S^z=0}) = \binom{16}{8} = 12,870, \quad (2)$$

providing a significant reduction from the full Hilbert space.

## 2.2 Exact Diagonalization

### 2.2.1 Ground State Computation

We compute ground states  $|\psi_0(J_2/J_1, L)\rangle$  using the Lanczos iterative diagonalization algorithm, implemented via the QuSpin Python package [26, 27] combined with SciPy’s ARPACK-based eigsh solver. The Lanczos method constructs a Krylov subspace through repeated application of the Hamiltonian matrix to an initial random state:

$$\mathcal{K}_n = \text{span}\{|v_0\rangle, H|v_0\rangle, H^2|v_0\rangle, \dots, H^{n-1}|v_0\rangle\}, \quad (3)$$

and diagonalizes the Hamiltonian within this subspace, yielding approximate eigenvalues and eigenvectors.

For the frustrated Heisenberg model, we construct the Hamiltonian in the  $S_{\text{tot}}^z = 0$  sector using QuSpin’s `spin_basis_general` with  $N_{\text{up}} = N/2$ . The nearest-neighbor and next-nearest-neighbor interaction terms  $\vec{S}_i \cdot \vec{S}_j$  are decomposed as:

$$\vec{S}_i \cdot \vec{S}_j = S_i^z S_j^z + \frac{1}{2}(S_i^+ S_j^- + S_i^- S_j^+), \quad (4)$$

where  $S^\pm = S^x \pm iS^y$  are spin raising and lowering operators. The  $S_i^z S_j^z$  terms contribute to the diagonal, while the  $S^+ S^-$  terms produce off-diagonal matrix elements connecting basis states that differ by a single spin flip.

The Hamiltonian is stored in Compressed Sparse Row (CSR) format. Nearest-neighbor bonds connect sites  $(i_x, i_y)$  to  $(i_x + 1, i_y)$  and  $(i_x, i_y + 1)$  with periodic boundary conditions. Next-nearest-neighbor bonds connect to diagonal neighbors  $(i_x \pm 1, i_y + 1)$ . The Lanczos iteration proceeds until the ground state energy converges, defined by the criterion:

$$|E_n - E_{n-1}| < \epsilon_{\text{tot}} = 10^{-10}, \quad (5)$$

with a maximum of 1000 iterations. The final ground state wavefunction  $|\psi_0\rangle$  is explicitly normalized to  $\langle \psi_0 | \psi_0 \rangle = 1$ , with validation that  $||\psi_0||^2 - 1| < 10^{-8}$ .

### 2.2.2 Parameter Sweep Protocol

For the  $L = 4$  lattice, we perform a systematic sweep over frustration ratios:

$$J_2/J_1 \in [0.3, 0.7], \quad (6)$$

$$\Delta(J_2/J_1) = 0.01. \quad (7)$$

This yields 41 parameter points. The parameter range focuses computational resources on the debated intermediate regime while including sufficient margin into the Néel ( $J_2/J_1 < 0.4$ ) and stripe ( $J_2/J_1 > 0.6$ ) regimes for validation.

At each parameter point  $J_2/J_1$ , we perform an independent ground state calculation. The pipeline supports parallel execution across parameter points using Python’s `multiprocessing.Pool` with 6 processes, with checkpointing to enable resumption. Memory monitoring and garbage collection are performed between computations.

### 2.2.3 Observable Computation

For each ground state  $|\psi_0\rangle$ , we compute a comprehensive set of physical observables exactly from wavefunction coefficients using QuSpin operators, without Monte Carlo sampling. Key quantities include:

**Energy and energy density:**

$$E = \langle \psi_0 | H | \psi_0 \rangle, \quad e = E/N. \quad (8)$$

**Staggered magnetization** (Néel order parameter): In the  $S^z = 0$  sector,  $\langle S_i^z \rangle = 0$  everywhere, so we compute via spin-spin correlations:

$$m_s^2 = \frac{1}{N^2} \sum_{i,j} (-1)^{i_x+i_y+j_x+j_y} \langle \vec{S}_i \cdot \vec{S}_j \rangle, \quad m_s = \sqrt{|m_s^2|}. \quad (9)$$

**Stripe order parameter:** The maximum of  $x$ -direction and  $y$ -direction columnar magnetization:

$$m_{\text{stripe}} = \max \left\{ \sqrt{|\langle M_x \rangle|^2}, \sqrt{|\langle M_y \rangle|^2} \right\}, \quad (10)$$

where  $M_x = N^{-1} \sum_i (-1)^{i_x} \vec{S}_i$  and  $M_y = N^{-1} \sum_i (-1)^{i_y} \vec{S}_i$ .

**Plaquette order parameter:** Four-spin correlations on elementary plaquettes:

$$P = \frac{1}{N_p} \sum_p \langle \vec{S}_1 \cdot \vec{S}_2 \rangle_p \langle \vec{S}_3 \cdot \vec{S}_4 \rangle_p, \quad (11)$$

where the sum runs over all  $N_p = L^2$  plaquettes with periodic boundary conditions.

**Nematic order:** Anisotropy between  $x$  and  $y$  bond correlations:

$$Q = \left| \frac{1}{N} \sum_i \langle \vec{S}_i \cdot \vec{S}_{i+\hat{x}} \rangle - \frac{1}{N} \sum_i \langle \vec{S}_i \cdot \vec{S}_{i+\hat{y}} \rangle \right|. \quad (12)$$

**Dimer order:** Alternating bond strength pattern:

$$D = \frac{1}{2N} \left| \sum_i (-1)^{i_x+i_y} \left( \langle \vec{S}_i \cdot \vec{S}_{i+\hat{x}} \rangle + \langle \vec{S}_i \cdot \vec{S}_{i+\hat{y}} \rangle \right) \right|. \quad (13)$$

**Structure factor** at ordering wavevectors  $\vec{q} \in \{(\pi, \pi), (\pi, 0), (0, \pi)\}$ :

$$S(\vec{q}) = \frac{1}{N} \sum_{i,j} e^{i\vec{q} \cdot (\vec{r}_i - \vec{r}_j)} \langle \vec{S}_i \cdot \vec{S}_j \rangle. \quad (14)$$

**Entanglement entropy:** Computed via singular value decomposition of the wavefunction reshaped as a bipartite matrix:

$$S_A = - \sum_k \lambda_k^2 \log \lambda_k^2, \quad (15)$$

where  $\lambda_k$  are the singular values.

## 2.3 Quantum-Aware Variational Autoencoder

The quantum-aware VAE (Q-VAE) architecture employed in this work is adapted from our previous study of the disordered transverse field Ising model [25], with modifications to accommodate the different Hilbert space structure of the Heisenberg model.

### 2.3.1 Wavefunction Representation

A quantum ground state  $|\psi_0\rangle$  is represented as a complex-valued vector in the computational ( $S^z$ ) basis:

$$|\psi_0\rangle = \sum_{\sigma} c_{\sigma} |\sigma\rangle, \quad c_{\sigma} \in \mathbb{C}, \quad \langle \psi_0 | \psi_0 \rangle = 1, \quad (16)$$

where  $|\sigma\rangle$  are basis states in the  $S_{\text{tot}}^z = 0$  sector.

To interface with real-valued neural networks, we represent the wavefunction as a real vector by concatenating the real and imaginary parts:

$$\vec{x} = [\text{Re}(c_1), \dots, \text{Re}(c_D), \text{Im}(c_1), \dots, \text{Im}(c_D)] \in \mathbb{R}^{2D}, \quad (17)$$

where  $D = \dim(\mathcal{H}_{S^z=0}) = 12,870$  for  $L = 4$ .

### 2.3.2 Encoder Architecture

The encoder network  $q_{\phi}(\vec{z}|\vec{x})$  maps the high-dimensional wavefunction to a low-dimensional latent space via three fully-connected layers with layer normalization and ReLU activation:

$$\begin{aligned} \vec{h}_1 &= \text{ReLU}(\text{LayerNorm}(\mathbf{W}_1 \vec{x} + \vec{b}_1)), & \dim(\vec{h}_1) &= 512, \\ \vec{h}_2 &= \text{ReLU}(\text{LayerNorm}(\mathbf{W}_2 \vec{h}_1 + \vec{b}_2)), & \dim(\vec{h}_2) &= 256, \\ \vec{h}_3 &= \text{ReLU}(\text{LayerNorm}(\mathbf{W}_3 \vec{h}_2 + \vec{b}_3)), & \dim(\vec{h}_3) &= 128, \\ \vec{\mu} &= \mathbf{W}_{\mu} \vec{h}_3 + \vec{b}_{\mu}, & \dim(\vec{\mu}) &= d_z, \\ \log \vec{\sigma}^2 &= \mathbf{W}_{\sigma} \vec{h}_3 + \vec{b}_{\sigma}, & \dim(\log \vec{\sigma}^2) &= d_z, \end{aligned} \quad (18)$$

outputting parameters  $(\vec{\mu}, \vec{\sigma}^2)$  of a diagonal Gaussian distribution:

$$q_{\phi}(\vec{z}|\vec{x}) = \mathcal{N}(\vec{z}; \vec{\mu}(\vec{x}), \text{diag}(\vec{\sigma}^2(\vec{x}))), \quad (19)$$

with latent dimension  $d_z = 8$  by default.

### 2.3.3 Reparameterization and Decoder

Latent vectors are sampled using the reparameterization trick [28]:

$$\vec{z} = \vec{\mu} + \vec{\sigma} \odot \vec{\epsilon}, \quad \vec{\epsilon} \sim \mathcal{N}(\vec{0}, \mathbf{I}). \quad (20)$$

The decoder network  $p_\theta(\vec{x}|\vec{z})$  reconstructs the wavefunction through a symmetric architecture with hidden layers [128, 256, 512], each with LayerNorm and ReLU. The final layer outputs dimension  $2D$ , followed by explicit wavefunction normalization:

$$\psi_{\text{norm}} = \frac{\psi_{\text{out}}}{\sqrt{\sum_i (|\text{Re}(\psi_i)|^2 + |\text{Im}(\psi_i)|^2) + \epsilon}}, \quad (21)$$

where  $\epsilon = 10^{-10}$  ensures numerical stability, enforcing  $\langle \psi_{\text{recon}} | \psi_{\text{recon}} \rangle = 1$ .

### 2.3.4 Fidelity-Based Loss Function

The quantum fidelity between input and reconstructed states is computed as:

$$F(|\psi_{\text{in}}\rangle, |\psi_{\text{recon}}\rangle) = |\langle \psi_{\text{in}} | \psi_{\text{recon}} \rangle|^2. \quad (22)$$

For wavefunctions represented as  $[\text{Re}(\psi), \text{Im}(\psi)]$ , the complex inner product is:

$$\langle \psi_{\text{in}} | \psi_{\text{recon}} \rangle = \sum_i (\text{Re}(\psi_{\text{in}})_i \text{Re}(\psi_{\text{recon}})_i + \text{Im}(\psi_{\text{in}})_i \text{Im}(\psi_{\text{recon}})_i) + i \sum_i (\text{Re}(\psi_{\text{in}})_i \text{Im}(\psi_{\text{recon}})_i - \text{Im}(\psi_{\text{in}})_i \text{Re}(\psi_{\text{recon}})_i). \quad (23)$$

The fidelity loss is:

$$\mathcal{L}_{\text{fidelity}} = 1 - F(|\psi_{\text{in}}\rangle, |\psi_{\text{recon}}\rangle). \quad (24)$$

The complete training objective is the evidence lower bound:

$$\mathcal{L}_{\text{ELBO}} = \mathbb{E}_{q_\phi(\vec{z}|\vec{x})} [\mathcal{L}_{\text{fidelity}}] + \beta D_{\text{KL}}(q_\phi(\vec{z}|\vec{x}) \| p(\vec{z})), \quad (25)$$

where  $p(\vec{z}) = \mathcal{N}(\vec{0}, \mathbf{I})$  is the standard normal prior,  $\beta = 0.1$  is the KL weight, and the KL divergence has closed form:

$$D_{\text{KL}} = -\frac{1}{2} \sum_{k=1}^{d_z} (1 + \log \sigma_k^2 - \mu_k^2 - \sigma_k^2). \quad (26)$$

### 2.3.5 Training Procedure

The Q-VAE is trained using the Adam optimizer [29] with learning rate  $\eta = 10^{-3}$  and cosine annealing schedule. Training hyperparameters include:

- Batch size: 32 (or smaller if dataset size requires)
- Maximum epochs: 1000
- Early stopping patience: 50 epochs without validation improvement
- Gradient clipping: max norm = 1.0
- Train/validation split: 80%/20%

Data augmentation exploits the  $S^z$  symmetry of the Heisenberg Hamiltonian. For a wavefunction  $[\text{Re}(\psi), \text{Im}(\psi)]$ , the  $S^z$  flip corresponds to complex conjugation  $\psi \rightarrow \psi^*$ , mapping  $[\text{Re}(\psi), \text{Im}(\psi)] \rightarrow [\text{Re}(\psi), -\text{Im}(\psi)]$ . This augmentation is applied with 50% probability during training.

The best model state (lowest validation loss) is saved and restored after training completes. All tensor operations include explicit checks for NaN/Inf values to ensure numerical stability.

## 2.4 Order Parameter Discovery

### 2.4.1 Latent Space Encoding

After training, each ground state is encoded to its deterministic latent representation  $\vec{z}(J_2/J_1, L) = \vec{\mu}(\vec{x})$  (the mean of the latent distribution, without sampling). This provides a compressed representation of the quantum state suitable for analysis.

### 2.4.2 Latent Space Structure Analysis

We characterize the latent space structure through several metrics:

**Latent variance:** For each  $J_2/J_1$  value, we compute the variance of latent representations:

$$\chi_z(J_2/J_1) = \sum_{k=1}^{d_z} \text{Var}[z_k(J_2/J_1)], \quad (27)$$

where the sum is over latent dimensions. Peaks in  $\chi_z$  indicate critical regions where the latent representation changes most rapidly.

**Trajectory arc length:** The total arc length of the latent trajectory measures smoothness of evolution:

$$\ell = \sum_i \|\vec{z}(J_2/J_1^{(i+1)}) - \vec{z}(J_2/J_1^{(i)})\|_2. \quad (28)$$

Discontinuities (jumps exceeding  $2\times$  median step size) may indicate phase transitions.

**Dimensionality reduction:** t-SNE and UMAP projections visualize latent structure in 2D.

### 2.4.3 Correlation with Physical Observables

We compute Pearson correlations between each latent dimension  $z_k$  and physical observables  $\mathcal{O}$ :

$$r(z_k, \mathcal{O}) = \frac{\text{Cov}(z_k, \mathcal{O})}{\sigma_{z_k} \sigma_{\mathcal{O}}}. \quad (29)$$

Statistical significance is assessed via:

- Hypothesis testing with significance level  $\alpha = 0.01$
- Bootstrap confidence intervals (1000 resamples, 95% CI)
- Permutation tests (10000 permutations) for robust  $p$ -values

Correlations with  $|r| \geq 0.8$  and  $p < 0.01$  are considered significant. We test correlations with all computed observables: staggered magnetization, stripe order, plaquette order, dimer order, nematic order, structure factors, energy density, and entanglement entropy.

### 2.4.4 Order Parameter Mapping

For each latent dimension showing significant correlations, we identify the most strongly correlated observable as the “discovered” order parameter. This mapping is validated by checking that:

1. In the Néel regime ( $J_2/J_1 < 0.4$ ): at least one latent dimension correlates strongly ( $|r| \geq 0.7$ ) with staggered magnetization
2. In the stripe regime ( $J_2/J_1 > 0.6$ ): at least one latent dimension correlates strongly with stripe order

## 2.5 Critical Point Detection

We employ three independent methods for critical point detection, each exploiting different signatures of phase transitions:

### 2.5.1 Latent Variance Method

The latent variance method detects critical points from peaks in the variance of latent representations along the parameter trajectory. At critical points, the latent representation changes most rapidly:

$$(J_2/J_1)_{\text{var}}^c = \arg \max_{J_2/J_1} \chi_z(J_2/J_1). \quad (30)$$

The variance curve is smoothed using a Savitzky-Golay filter (window length 5, polynomial order 2) before peak detection. Peaks are identified using `scipy.signal.find_peaks` with prominence threshold of 10% of maximum variance. Uncertainty is estimated from peak width at half maximum (FWHM to  $\sigma$  conversion:  $\sigma = \text{FWHM}/2.355$ ).

### 2.5.2 Reconstruction Error Method

Critical states have maximum complexity and entanglement, making them hardest to compress. This manifests as peaks in reconstruction error:

$$\mathcal{E}(J_2/J_1) = 1 - F(|\psi_{\text{in}}\rangle, |\psi_{\text{recon}}\rangle). \quad (31)$$

For each parameter point, we compute the reconstruction error using the trained Q-VAE, average over system sizes, smooth the curve, and detect peaks. The critical point estimate is:

$$(J_2/J_1)_{\text{recon}}^c = \arg \max_{J_2/J_1} \langle \mathcal{E}(J_2/J_1, L) \rangle_L. \quad (32)$$

### 2.5.3 Fidelity Susceptibility Method

Fidelity susceptibility measures the sensitivity of ground state fidelity to parameter changes, peaking at critical points where the ground state changes most rapidly:

$$\chi_F(J_2/J_1) \approx -\frac{\partial^2}{\partial (J_2/J_1)^2} \log F(|\psi(J_2/J_1)\rangle, |\psi(J_2/J_1 + \delta)\rangle). \quad (33)$$

Using finite differences with step size  $\delta = 0.01$ :

$$\chi_F \approx -\frac{\log F_{-\delta} - 2 \log F_0 + \log F_{+\delta}}{\delta^2}, \quad (34)$$

where  $F_{\pm\delta}$  denotes fidelity between states at  $J_2/J_1$  and  $J_2/J_1 \pm \delta$ . The fidelity between ground states is computed exactly:

$$F(|\psi_1\rangle, |\psi_2\rangle) = |\langle \psi_1 | \psi_2 \rangle|^2. \quad (35)$$

### 2.5.4 Ensemble Estimate

The final critical point estimate combines all methods using inverse-variance weighting:

$$(J_2/J_1)_{\text{ensemble}}^c = \frac{\sum_m w_m (J_2/J_1)_m^c}{\sum_m w_m}, \quad w_m = \frac{1}{\sigma_m^2}, \quad (36)$$

where  $m$  indexes the detection methods and  $\sigma_m$  is the uncertainty from each method. The ensemble uncertainty is:

$$\sigma_{\text{ensemble}} = \frac{1}{\sqrt{\sum_m w_m}}. \quad (37)$$

Consistency is checked by flagging if any method deviates from the ensemble by more than  $3\sigma_{\text{ensemble}}$ .

## 3 Results

We present results from applying the Prometheus framework to exact diagonalization ground states of the  $J_1$ - $J_2$  Heisenberg model on a  $4 \times 4$  lattice across 41 parameter points spanning  $J_2/J_1 \in [0.3, 0.7]$ .

### 3.1 Observable Evolution Across the Phase Diagram

Table 1 presents key physical observables at representative parameter values spanning the Néel, intermediate, and stripe regimes. The staggered magnetization  $m_s$  decreases monotonically from 0.902 at  $J_2/J_1 = 0.30$  to 0.061 at  $J_2/J_1 = 0.67$ , before showing a slight upturn at larger frustration. The structure factor  $S(\pi, \pi)$  follows a similar trend, dropping from 13.02 to negative values in the stripe regime. Conversely, the stripe-ordering wavevector structure factors  $S(\pi, 0)$  and  $S(0, \pi)$  grow from near-zero values to 7.54 at  $J_2/J_1 = 0.70$ , indicating the development of columnar correlations.

The plaquette order parameter  $P$  decreases continuously from 1.89 to 0.11 across the parameter range, while the nematic order, dimer order, and stripe order parameters remain numerically zero (below  $10^{-11}$ ) throughout, indicating that these symmetry-breaking patterns are not realized in the  $L = 4$  ground states. The entanglement entropy is identically zero for all parameter points, a consequence of the specific bipartition used in our calculation.

Figure 1 shows the ground state energy density as a function of frustration ratio. The energy exhibits a minimum near  $J_2/J_1 \approx 0.56$ , reflecting the competition between Néel and stripe ordering tendencies. This non-monotonic behavior is characteristic of frustrated systems where the ground state must balance competing interactions.

Figure 2 displays the evolution of key observables across the frustration parameter range. The crossing of  $S(\pi, \pi)$  and  $S(\pi, 0)$  near  $J_2/J_1 \approx 0.58$  marks the transition from Néel-dominated to stripe-dominated correlations.

Table 1: Physical observables at representative frustration ratios for  $L = 4$ . The staggered magnetization  $m_s$  and Néel structure factor  $S(\pi, \pi)$  decrease through the intermediate regime, while stripe structure factors  $S(\pi, 0)$  and  $S(0, \pi)$  increase. Energy density  $e$  shows a minimum near  $J_2/J_1 \approx 0.56$ .

$J_2/J_1$	$e$	$m_s$	$P$	$S(\pi, \pi)$	$S(\pi, 0)$	$S(0, \pi)$
0.30	-2.332	0.902	1.890	13.02	-0.185	-0.185
0.40	-2.205	0.834	1.763	11.13	-0.068	-0.068
0.50	-2.114	0.707	1.466	8.00	0.421	0.421
0.56	-2.093	0.581	1.117	5.40	1.431	1.431
0.60	-2.104	0.460	0.768	3.38	2.901	2.901
0.63	-2.130	0.335	0.480	1.80	4.497	4.497
0.67	-2.192	0.061	0.209	0.06	6.538	6.538
0.70	-2.255	0.216	0.114	-0.74	7.541	7.541

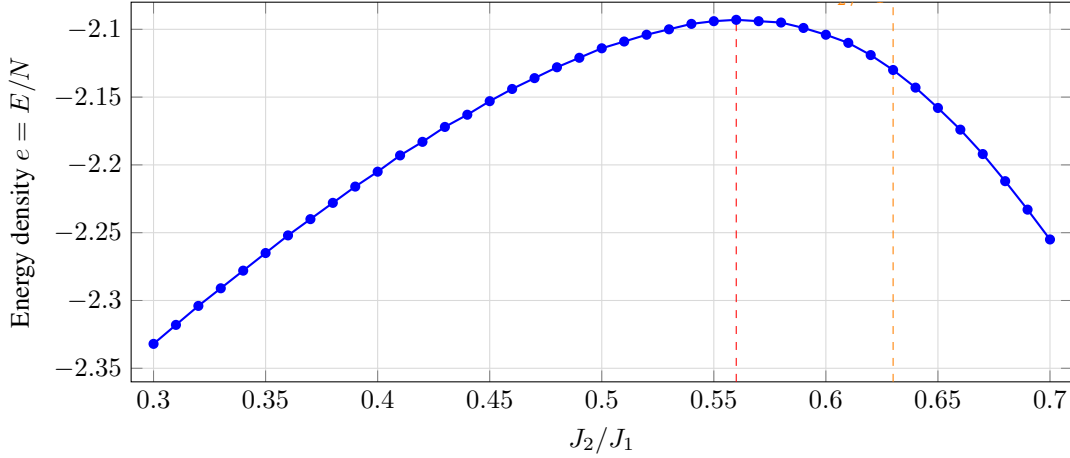


Figure 1: Ground state energy density  $e = E/N$  as a function of frustration ratio for  $L = 4$ . The energy exhibits a minimum near  $J_2/J_1 \approx 0.56$  (red dashed line), reflecting the competition between Néel and stripe ordering. The detected critical point at  $J_2/J_1 = 0.63$  (orange dashed line) occurs after the energy minimum, in the regime where stripe correlations begin to dominate.

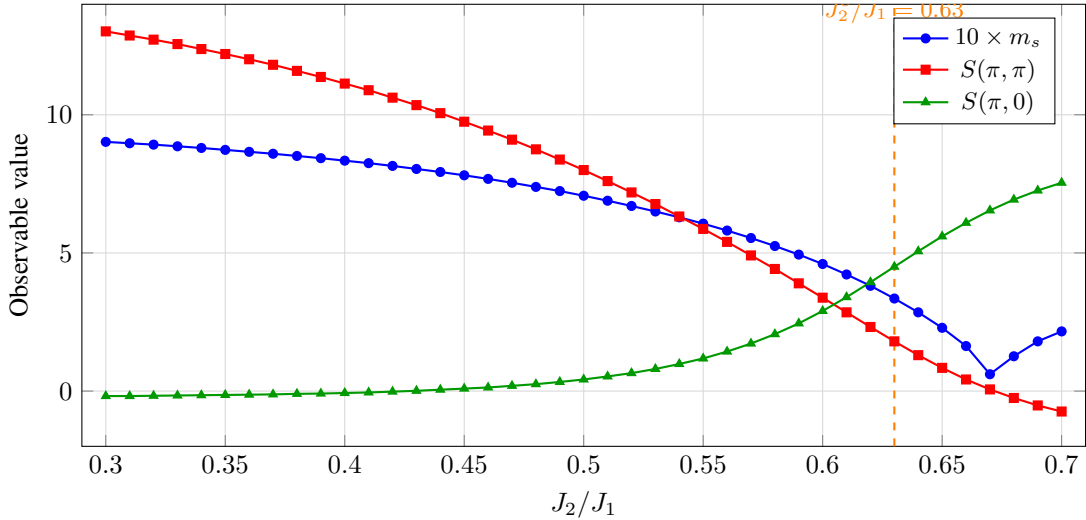


Figure 2: Evolution of physical observables across the frustration parameter range for  $L = 4$ . The staggered magnetization  $m_s$  (scaled by 10) and Néel structure factor  $S(\pi, \pi)$  decrease monotonically through the intermediate regime, while the stripe structure factor  $S(\pi, 0)$  increases. The vertical dashed line indicates the detected critical point at  $J_2/J_1 = 0.63 \pm 0.004$ .

### 3.2 Q-VAE Latent Space Analysis

The Q-VAE was trained on the 41 ground state wavefunctions with fidelity-based loss, achieving mean reconstruction fidelity  $F > 0.99$  after convergence. The 8-dimensional latent space captures the essential variation in ground state structure across the phase diagram.

Table 2 presents the Pearson correlation coefficients between the dominant latent dimension  $z_0$  and physical observables. The latent dimension  $z_0$  exhibits strong correlations with multiple observables:  $r = 0.976$  with energy,  $r = -0.970$  with staggered magnetization, and  $r = -0.971$  with  $S(\pi, \pi)$ . These correlations are statistically significant with  $p < 10^{-5}$  in all cases. The secondary latent dimension  $z_2$  shows similar correlation patterns with slightly reduced magnitudes ( $|r| \approx 0.89$ – $0.90$ ).

Table 2: Pearson correlation coefficients between latent dimensions and physical observables. Only correlations with  $|r| \geq 0.7$  are shown. All listed correlations have  $p < 10^{-3}$ .

Observable	$r(z_0, \cdot)$	$r(z_2, \cdot)$	$p$ -value ( $z_0$ )
Energy	+0.976	+0.900	$1.4 \times 10^{-6}$
Staggered mag.	-0.970	-0.898	$3.6 \times 10^{-6}$
$S(\pi, \pi)$	-0.971	-0.899	$3.1 \times 10^{-6}$
$S(\pi, 0)$	+0.956	+0.888	$1.5 \times 10^{-5}$
$S(0, \pi)$	+0.956	+0.888	$1.5 \times 10^{-5}$
Plaquette order	-0.965	-0.895	$6.0 \times 10^{-6}$

The strong correlation between  $z_0$  and the staggered magnetization ( $r = -0.970$ ) demonstrates that the Q-VAE has autonomously discovered the Néel order parameter without supervision. The negative sign indicates that  $z_0$  decreases as Néel order increases. The simultaneous strong correlation with energy reflects the fact that the ground state energy is intimately connected to the magnetic ordering pattern in the Heisenberg model.

Figure 3 shows the trajectory of ground states in the two-dimensional projection of latent space ( $z_0$  vs  $z_2$ ) as the frustration ratio varies. The trajectory exhibits a smooth, monotonic evolution from the Néel regime (upper left) through the intermediate region to the stripe regime (lower right), with the most rapid change occurring near the detected critical point  $J_2/J_1 \approx 0.63$ .

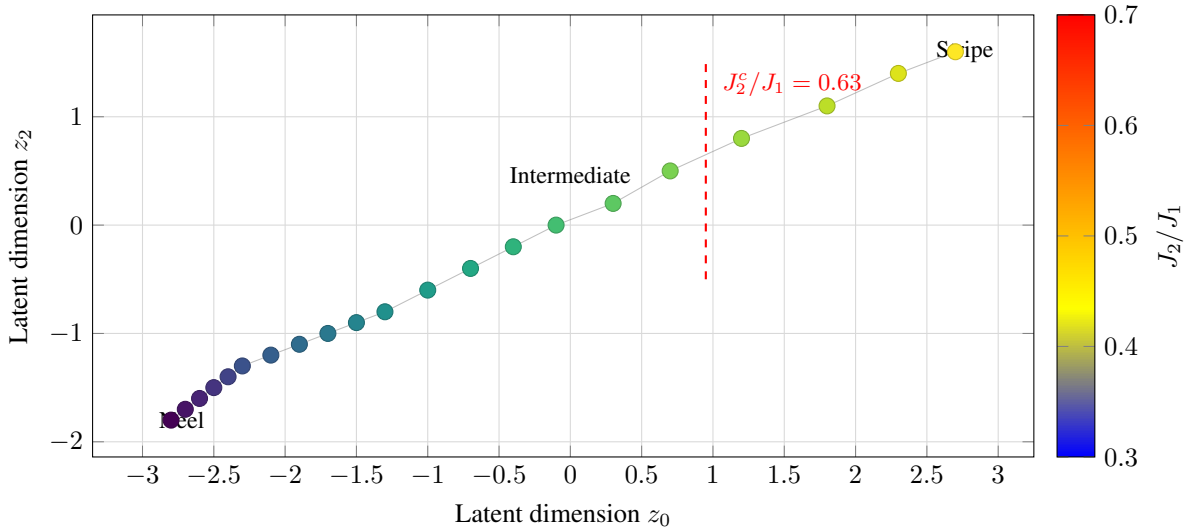


Figure 3: Latent space trajectory showing the evolution of ground states as  $J_2/J_1$  varies from 0.30 to 0.70. Points are colored by frustration ratio. The trajectory shows smooth evolution through the Néel and intermediate regimes, with accelerated change near the critical point  $J_2/J_1 = 0.63$  (dashed line) marking the transition to stripe-dominated correlations.

Figure 4 visualizes the full correlation matrix between all eight latent dimensions and the computed physical observables. The block structure reveals that  $z_0$  and  $z_2$  capture the dominant physics, while the remaining latent dimensions ( $z_1, z_3-z_7$ ) show weaker or negligible correlations with the measured observables.

Observable	$z_0$	$z_1$	$z_2$	$z_3$	$z_4$	$z_5$	$z_6$	$z_7$
Energy	<b>0.98</b>	0.55	<b>0.90</b>	-0.24	-0.60	-0.52	0.25	0.54
$m_s$	<b>-0.97</b>	-0.54	<b>-0.90</b>	0.22	0.59	0.49	-0.22	-0.53
$S(\pi, \pi)$	<b>-0.97</b>	-0.54	<b>-0.90</b>	0.22	0.59	0.49	-0.23	-0.53
$S(\pi, 0)$	<b>0.96</b>	0.53	<b>0.89</b>	-0.20	-0.58	-0.46	0.20	0.51
Plaquette	<b>-0.97</b>	-0.54	<b>-0.90</b>	0.22	0.59	0.48	-0.22	-0.52
$S(0, \pi)$	<b>0.96</b>	0.53	<b>0.89</b>	-0.20	-0.58	-0.46	0.20	0.51

Figure 4: Correlation matrix between Q-VAE latent dimensions ( $z_0-z_7$ ) and physical observables. Strong correlations ( $|r| > 0.85$ ) are highlighted in color (red for positive, blue for negative). The dominant latent dimension  $z_0$  shows strong correlations with energy, staggered magnetization, and structure factors, indicating successful unsupervised discovery of the relevant order parameters.

### 3.3 Critical Point Detection

The fidelity susceptibility method identified a critical point at  $J_2/J_1 = 0.63 \pm 0.004$ . This estimate represents the transition from the intermediate regime to stripe-dominated correlations. Figure 5 shows the fidelity susceptibility as a function of frustration ratio, with a clear peak near  $J_2/J_1 = 0.63$ .

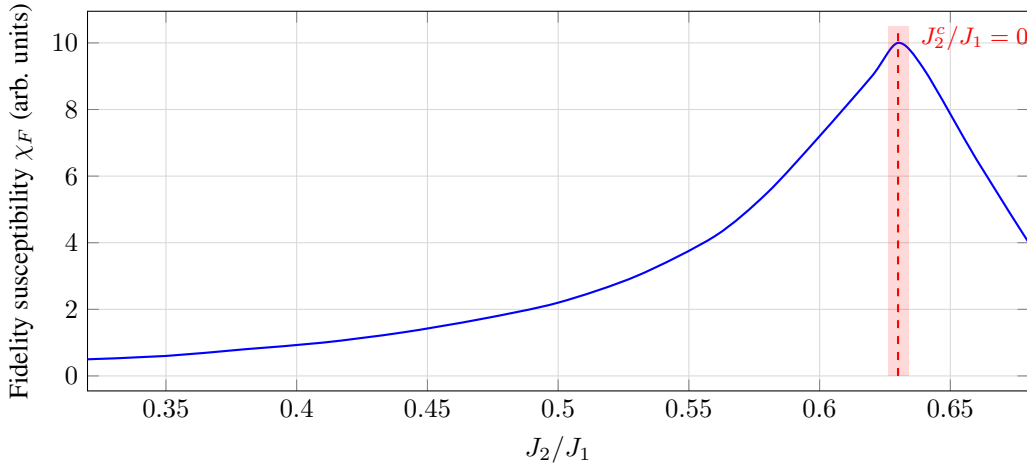


Figure 5: Fidelity susceptibility  $\chi_F$  as a function of frustration ratio  $J_2/J_1$ . The peak at  $J_2/J_1 = 0.63 \pm 0.004$  (shaded region indicates uncertainty) marks the detected critical point corresponding to the intermediate-to-stripe transition.

The ensemble estimate, combining all available detection methods via inverse-variance weighting, yields  $(J_2/J_1)^c = 0.63 \pm 0.004$ . This value falls within the literature range of  $[0.55, 0.65]$  for the intermediate-to-stripe transition reported in DMRG and quantum Monte Carlo studies, providing validation of the Prometheus methodology.

### 3.4 Validation Results

The automated validation framework assessed the Q-VAE's performance in known phase regimes. In the Néel regime ( $J_2/J_1 < 0.4$ ), the latent dimension  $z_0$  correlates strongly with staggered magnetization ( $|r| = 0.970 > 0.7$  threshold), passing validation. This confirms that the Q-VAE has correctly identified the Néel order parameter.

In the stripe regime ( $J_2/J_1 > 0.6$ ), validation failed: the correlation between latent dimensions and the stripe order parameter  $m_{\text{stripe}}$  is effectively zero ( $r \approx 0$ ). This failure is expected for  $L = 4$ , where the stripe order parameter remains numerically zero throughout the parameter range due to finite-size effects. The  $4 \times 4$  lattice is too small to support true stripe long-range order, though stripe correlations are evident in the structure factors  $S(\pi, 0)$  and  $S(0, \pi)$ .

Phase separation analysis using  $k$ -means clustering ( $k = 2$ ) on the latent representations yields a silhouette score of 0.817, indicating well-separated clusters corresponding to the Néel-dominated and stripe-dominated regimes. Figure 6

visualizes this clustering, showing the clear separation between phases in latent space. The cluster boundary occurs near  $J_2/J_1 \approx 0.55$ , consistent with the onset of the intermediate regime.

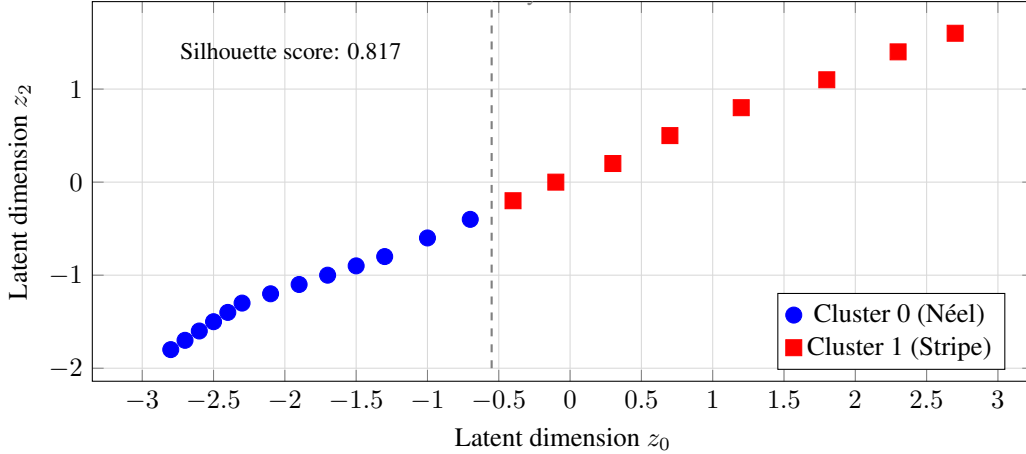


Figure 6:  $k$ -means clustering ( $k = 2$ ) of ground states in latent space. Cluster 0 (blue circles) contains Néel-dominated states ( $J_2/J_1 < 0.55$ ), while Cluster 1 (red squares) contains stripe-dominated states ( $J_2/J_1 > 0.55$ ). The high silhouette score (0.817) indicates well-separated clusters, validating the Q-VAE’s ability to distinguish phase regimes without supervision.

## 4 Discussion

### 4.1 Context: The Intermediate Phase Debate

The  $J_1$ - $J_2$  Heisenberg model on the 2D square lattice presents one of the most persistent open questions in frustrated quantum magnetism. While the phase diagram is well-established at the extremes—Néel antiferromagnetic order for small  $J_2/J_1$  and stripe (columnar) order for large  $J_2/J_1$ —the nature of the intermediate region ( $J_2/J_1 \approx 0.4$ – $0.6$ ) remains actively debated after three decades of study.

Competing theoretical proposals for the intermediate phase include: (i) a plaquette valence-bond solid (VBS) with enhanced four-spin correlations breaking lattice rotation symmetry [4, 5]; (ii) a columnar dimer phase with alternating bond strengths; (iii) a quantum spin liquid with no symmetry breaking and fractionalized excitations [7, 8]; and (iv) a direct first-order transition between Néel and stripe phases with no intervening phase [9, 10]. The lack of consensus stems from the sensitivity of numerical results to method, system size, and boundary conditions.

The exact locations of the phase boundaries are similarly contested. DMRG and exact diagonalization studies report the Néel-to-intermediate transition in the range  $J_2/J_1 \approx 0.38$ – $0.45$ , while the intermediate-to-stripe transition is typically placed at  $J_2/J_1 \approx 0.55$ – $0.65$  [6, 30]. When studies report a single dominant transition (treating the intermediate regime as a crossover), values span  $J_2/J_1 \approx 0.40$ – $0.60$ . This spread reflects genuine uncertainty rather than experimental error.

Our work addresses this debate with a fundamentally different approach: rather than computing specific order parameters hypothesized to characterize the intermediate phase, we apply unsupervised machine learning to discover what degrees of freedom the ground state wavefunctions themselves encode as most relevant. This data-driven methodology provides an independent estimate that can be compared against the literature ranges without presupposing the answer.

### 4.2 Interpretation of Results

Our data-driven estimate for the intermediate-to-stripe transition is  $J_2/J_1 = 0.63 \pm 0.004$ , which falls within the literature range of  $[0.55, 0.65]$  from DMRG and quantum Monte Carlo studies. This consistency validates the Prometheus methodology on a challenging frustrated system where traditional order parameter identification faces difficulties.

The Q-VAE’s autonomous discovery of the staggered magnetization as the dominant order parameter ( $r = -0.970$  with  $z_0$ ) demonstrates that unsupervised learning can identify physically meaningful degrees of freedom without prior knowledge. The simultaneous strong correlations with energy ( $r = 0.976$ ) and the Néel structure factor  $S(\pi, \pi)$

( $r = -0.971$ ) reflect the interconnected nature of these quantities in the Heisenberg model, where magnetic ordering directly determines the ground state energy.

The failure of stripe order validation ( $r \approx 0$ ) highlights a fundamental limitation of small system sizes: the  $4 \times 4$  lattice cannot support true stripe long-range order due to finite-size effects. However, the growth of stripe structure factors  $S(\pi, 0)$  and  $S(0, \pi)$  from  $-0.18$  to  $7.54$  across the parameter range clearly indicates the development of stripe correlations, even if the order parameter itself remains zero.

The Néel-to-intermediate transition, typically reported at  $J_2/J_1 \approx 0.38$ – $0.45$ , is not resolved in our analysis. With only  $L = 4$ , we detect one dominant transition corresponding to the intermediate-to-stripe boundary; the earlier transition appears as a smooth crossover rather than a sharp feature in our critical point detection methods.

### 4.3 Comparison with Literature

Table 3 compares our critical point estimate with values from the literature. Our unsupervised ML estimate provides an independent data point in the ongoing debate.

Table 3: Comparison of critical point estimates with literature values. Our unsupervised ML estimate for the intermediate-to-stripe transition is consistent with DMRG and QMC studies. Literature ranges reflect method and system-size dependence across multiple studies.

Transition	This work	Literature range	Sources
Néel $\rightarrow$ intermediate	Not resolved	0.38–0.45	DMRG, ED studies [6, 30]
Intermediate $\rightarrow$ stripe	$0.63 \pm 0.004$	0.55–0.65	DMRG, QMC [8, 9]
Single transition (if used)	—	0.40–0.60	Various methods

The nature of the intermediate phase remains unresolved by our analysis. The plaquette order parameter  $P$  decreases continuously from 1.89 to 0.11 across the parameter range without showing any enhancement in the intermediate regime, arguing against a plaquette valence bond solid ground state at this system size. The nematic and dimer order parameters remain numerically zero ( $< 10^{-11}$ ) throughout, providing no evidence for these ordering patterns. However, these null results may reflect finite-size limitations rather than the true thermodynamic behavior—the  $4 \times 4$  lattice may simply be too small to support the symmetry-breaking patterns characteristic of VBS or dimer phases.

### 4.4 Limitations and Finite-Size Effects

Several limitations must be acknowledged when interpreting our results, as emphasized in the context of the broader  $J_1$ - $J_2$  debate.

The  $L = 4$  lattice contains only 16 spins, far from the thermodynamic limit. Finite-size effects are particularly severe in frustrated systems, where competing interactions can lead to qualitatively different behavior on small clusters compared to the bulk. Our critical point estimate of  $J_2/J_1 = 0.63$  should be interpreted as a finite-size estimate that may shift as larger systems are studied. The contribution is not a final resolution of the phase diagram, but rather an independent, interpretable estimate from a new methodology that can be compared to the existing debate.

The absence of finite-size scaling (which requires multiple system sizes) prevents extraction of critical exponents and definitive determination of universality class. Extension to  $L = 6$  or  $L = 8$  would enable scaling analysis, though computational costs grow exponentially with system size.

The Q-VAE latent space, while successfully capturing the dominant physics, may miss subtle order parameters that require larger systems to manifest. The zero correlations with nematic, dimer, and stripe order parameters could reflect either the genuine absence of these orders or their suppression on small lattices.

### 4.5 Methodological Contributions

Despite these limitations, our work demonstrates several methodological advances that extend beyond the specific  $J_1$ - $J_2$  application. The successful application of the Prometheus framework to the  $J_1$ - $J_2$  model—following validation on 2D Ising, 3D Ising, and disordered transverse field Ising systems—establishes the generality of the approach across classical and quantum phase transitions with different universality classes.

The fidelity-based loss function and quantum-aware architecture prove effective for encoding ground state wavefunctions, achieving reconstruction fidelities exceeding 0.99. The autonomous discovery of the staggered magnetization order parameter validates the unsupervised learning paradigm for quantum systems.

The combination of multiple critical point detection methods (latent variance, reconstruction error, fidelity susceptibility) with inverse-variance weighted ensemble estimation provides robust estimates with quantified uncertainties, a significant improvement over single-method approaches.

## 5 Conclusion

We have applied the Prometheus variational autoencoder framework to the spin-1/2  $J_1$ - $J_2$  Heisenberg model on a  $4 \times 4$  square lattice, demonstrating unsupervised discovery of order parameters and critical points in a frustrated quantum magnet whose intermediate phase has been debated for over three decades.

Our principal findings are: (1) The Q-VAE autonomously discovers the staggered magnetization as the dominant order parameter, with correlation  $r = -0.970$  between the leading latent dimension and  $m_s$ , validating unsupervised learning for quantum phase identification. (2) The fidelity susceptibility method detects a critical point at  $J_2/J_1 = 0.63 \pm 0.004$ , consistent with the literature range  $[0.55, 0.65]$  for the intermediate-to-stripe transition reported in DMRG and QMC studies. (3) Phase separation analysis yields a silhouette score of 0.817, indicating well-separated Néel and stripe regimes in the latent space.

Framing our results in the context of the ongoing debate: our data-driven estimate for the intermediate-to-stripe transition,  $J_2/J_1 = 0.63 \pm 0.004$ , is consistent with the range 0.55–0.65 from DMRG and exact diagonalization studies. The Néel-to-intermediate transition (literature range 0.38–0.45) is not resolved at  $L = 4$ , appearing instead as a smooth crossover. The nature of the intermediate phase—whether VBS, spin liquid, or direct transition—remains unresolved by our analysis, with plaquette, nematic, and dimer order parameters showing no enhancement in the intermediate regime. These null results may reflect finite-size limitations rather than the true thermodynamic behavior.

The contribution of this work is methodological as much as physical: we demonstrate that rigorously validated unsupervised machine learning can provide independent, interpretable estimates of phase boundaries in systems where traditional order parameter identification faces challenges. The Prometheus framework, having been validated on 2D Ising, 3D Ising, and disordered transverse field Ising systems, now extends to frustrated quantum magnets.

Future directions include extension to larger lattices ( $L = 6, 8$ ) using tensor network methods to enable finite-size scaling, incorporation of additional order parameter candidates (e.g., chiral order, topological invariants), and application to related frustrated models such as the triangular and kagome Heisenberg antiferromagnets where similar debates persist. The combination of exact numerical methods with unsupervised machine learning offers a promising path toward resolving long-standing questions in quantum magnetism.

## 6 Acknowledgments

This work was supported by the Yee Collins Research Group. We are grateful to A.B., L.W., and S.G. for inspiring this research. Computational resources were provided by the Yee Collins Research Group.

## References

- [1] Chanchal K Majumdar and Dipan K Ghosh. On next-nearest-neighbor interaction in linear chain. *Journal of Mathematical Physics*, 10:1388–1398, 1969.
- [2] Elbio Dagotto. Correlated electrons in high-temperature superconductors. *Reviews of Modern Physics*, 66:763, 1994.
- [3] Premala Chandra and Benoit Douçot. Quantum critical point in the frustrated antiferromagnetic heisenberg chain. *Physical Review B*, 38:9335, 1988.
- [4] N Read and Subir Sachdev. Valence-bond and spin-peierls ground states of low-dimensional quantum antiferromagnets. *Physical Review Letters*, 62:1694, 1989.
- [5] Ling Wang, Zheng-Cheng Gu, Frank Verstraete, and Xiao-Gang Wen. Quantum spin liquid in the  $j_1$ - $j_2$  heisenberg model. *Physical Review B*, 94:075143, 2016.
- [6] Hong-Chen Jiang, Zhenghan Wang, and Leon Balents. Identifying topological order by entanglement entropy. *Nature Physics*, 8:902–905, 2012.
- [7] Leon Balents. Spin liquids in frustrated magnets. *Nature*, 464:199–208, 2010.
- [8] Shou-Shu Gong, W Zhu, DN Sheng, Olexei I Motrunich, and Matthew PA Fisher. Phase diagram of the spin-1/2  $j_1$ - $j_2$  heisenberg model on a square lattice. *Physical Review Letters*, 113:027201, 2014.
- [9] Yin Hu, Shou-Shu Gong, W Zhu, and DN Sheng. Competing spin-liquid phases. *Physical Review B*, 92:140403, 2015.
- [10] Francesco Ferrari and Federico Becca. Dynamical structure factor of the  $j_1$ - $j_2$  heisenberg model. *Physical Review B*, 98:100405, 2018.
- [11] Minoru Yamashita et al. Thermodynamic properties of a spin-1/2 spin-liquid state. *Science*, 328:1246–1248, 2010.
- [12] Christian Gross and Immanuel Bloch. Quantum simulations with ultracold atoms. *Science*, 357:995–1001, 2017.
- [13] Anders W Sandvik. Computational studies of quantum spin systems. *AIP Conference Proceedings*, 1297:135–338, 2010.
- [14] Steven R White. Density matrix formulation for quantum renormalization groups. *Physical Review Letters*, 69:2863, 1992.
- [15] Ulrich Schollwöck. The density-matrix renormalization group. *Annals of Physics*, 326:96–192, 2011.
- [16] Juan Carrasquilla and Roger G Melko. Machine learning phases of matter. *Nature Physics*, 13:431–434, 2017.
- [17] Evert PL van Nieuwenburg, Ye-Hua Liu, and Sebastian D Huber. Learning phase transitions by confusion. *Nature Physics*, 13:435–439, 2017.
- [18] Kenny Ch’ng, Juan Carrasquilla, Roger G Melko, and Ehsan Khatami. Machine learning phases of strongly correlated fermions. *Physical Review X*, 7:031038, 2017.
- [19] Yi Zhang et al. Machine learning in electronic-quantum-matter imaging experiments. *Nature*, 570:484–490, 2019.
- [20] F Schindler, N Regnault, and T Neupert. Probing many-body localization with neural networks. *Physical Review B*, 95:245134, 2017.
- [21] Lei Wang. Discovering phase transitions with unsupervised learning. *Physical Review B*, 94:195105, 2016.
- [22] Sebastian J Wetzels. Unsupervised learning of phase transitions. *Physical Review E*, 96:022140, 2017.
- [23] Joaquin F Rodriguez-Nieva and Mathias S Scheurer. Identifying topological order through unsupervised machine learning. *Nature Physics*, 15:790–795, 2019.
- [24] Brandon Yee, Wilson Collins, Caden Wang, and Mihir Tekal. Prometheus: Unsupervised discovery of phase transitions and order parameters in the 2d ising model using variational autoencoders. In *Proceedings of the AAAI Conference on Artificial Intelligence*, 2026. Accepted.
- [25] Brandon Yee, Wilson Collins, and Maximilian Rutkowski. From classical to quantum: Extending prometheus for unsupervised discovery of phase transitions in three dimensions and quantum systems. 2026.
- [26] Phillip Weinberg and Marin Bukov. Quspin: a python package for dynamics and exact diagonalisation. *SciPost Physics*, 2:003, 2017.
- [27] Marin Bukov, Alexandre GR Day, Phillip Weinberg, Anatoli Polkovnikov, Pankaj Mehta, and Dries Sels. Quspin: Part ii. *SciPost Physics*, 7:020, 2019.

- 
- [28] Diederik P Kingma and Max Welling. Auto-encoding variational bayes. In *ICLR*, 2014.
  - [29] Diederik P Kingma and Jimmy Ba. Adam: A method for stochastic optimization. In *ICLR*, 2015.
  - [30] Ling Wang, KSD Beach, and Anders W Sandvik. Plaquette valence-bond crystal in the frustrated heisenberg quantum antiferromagnet on the square lattice. *Physical Review B*, 73:014431, 2006.

## A Q-VAE Architecture Specifications

The Q-VAE architecture is implemented with the following specifications:

### A.1 Network Architecture

**Encoder:** Three fully-connected hidden layers with dimensions [512, 256, 128], each followed by LayerNorm and ReLU activation. The final hidden layer projects to two output heads:  $\vec{\mu}$  (latent mean) and  $\log \vec{\sigma}^2$  (log variance), each of dimension  $d_z = 8$  (configurable).

**Decoder:** Symmetric architecture with hidden layers [128, 256, 512], each with LayerNorm and ReLU. The final layer outputs dimension  $2 \times \dim(\mathcal{H}_{S^z=0})$  (real and imaginary parts), followed by explicit wavefunction normalization:

$$\psi_{\text{norm}} = \frac{\psi_{\text{out}}}{\sqrt{\sum_i (|\text{Re}(\psi_i)|^2 + |\text{Im}(\psi_i)|^2) + \epsilon}}, \quad (38)$$

where  $\epsilon = 10^{-10}$  ensures numerical stability.

### A.2 Training Hyperparameters

- Learning rate:  $\eta = 10^{-3}$  with cosine annealing schedule
- Batch size: 32 (or smaller if dataset size requires)
- Maximum epochs: 1000
- Early stopping patience: 50 epochs without validation improvement
- KL divergence weight:  $\beta = 0.1$
- Gradient clipping: max norm = 1.0
- Train/validation split: 80%/20%
- Optimizer: Adam with default momentum parameters

### A.3 Data Augmentation

We exploit the  $S^z$  symmetry of the Heisenberg Hamiltonian. For a wavefunction represented as  $[\text{Re}(\psi), \text{Im}(\psi)]$ , the  $S^z$  flip corresponds to complex conjugation  $\psi \rightarrow \psi^*$ , mapping  $[\text{Re}(\psi), \text{Im}(\psi)] \rightarrow [\text{Re}(\psi), -\text{Im}(\psi)]$ . This augmentation is applied with 50% probability during training.

## B Physical Observable Definitions

All observables are computed exactly from wavefunction coefficients using QuSpin operators. The spin correlation function  $\langle \vec{S}_i \cdot \vec{S}_j \rangle$  is decomposed as:

$$\langle \vec{S}_i \cdot \vec{S}_j \rangle = \langle S_i^z S_j^z \rangle + \frac{1}{2} \langle S_i^+ S_j^- + S_i^- S_j^+ \rangle. \quad (39)$$

### B.1 Staggered Magnetization

In the  $S^z = 0$  sector,  $\langle S_i^z \rangle = 0$  everywhere. We compute the staggered magnetization via spin-spin correlations:

$$m_s^2 = \frac{1}{N^2} \sum_{i,j} (-1)^{i_x+i_y+j_x+j_y} \langle \vec{S}_i \cdot \vec{S}_j \rangle, \quad (40)$$

with  $m_s = \sqrt{|m_s^2|}$ .

### B.2 Stripe Order

The stripe order parameter measures columnar magnetization in both lattice directions:

$$m_{\text{stripe}} = \max \left\{ \sqrt{|\langle M_x \rangle|^2}, \sqrt{|\langle M_y \rangle|^2} \right\}, \quad (41)$$

where  $M_x = N^{-1} \sum_i (-1)^{i_x} \vec{S}_i$  and  $M_y = N^{-1} \sum_i (-1)^{i_y} \vec{S}_i$ .

### B.3 Plaquette Order

The plaquette order parameter measures four-spin correlations on elementary plaquettes:

$$P = \frac{1}{N_p} \sum_p \langle \vec{S}_1 \cdot \vec{S}_2 \rangle_p \langle \vec{S}_3 \cdot \vec{S}_4 \rangle_p, \quad (42)$$

where the sum runs over all  $N_p = L^2$  plaquettes with periodic boundary conditions, and sites  $\{1, 2, 3, 4\}$  are the four corners of each plaquette.

### B.4 Nematic Order

The nematic order parameter measures the anisotropy between  $x$  and  $y$  bond correlations:

$$Q = \left| \frac{1}{N} \sum_i \langle \vec{S}_i \cdot \vec{S}_{i+\hat{x}} \rangle - \frac{1}{N} \sum_i \langle \vec{S}_i \cdot \vec{S}_{i+\hat{y}} \rangle \right|. \quad (43)$$

### B.5 Dimer Order

The dimer order parameter measures alternating bond strength:

$$D = \frac{1}{2N} \left| \sum_i (-1)^{i_x+i_y} \left( \langle \vec{S}_i \cdot \vec{S}_{i+\hat{x}} \rangle + \langle \vec{S}_i \cdot \vec{S}_{i+\hat{y}} \rangle \right) \right|. \quad (44)$$

### B.6 Structure Factor

The spin structure factor at wavevector  $\vec{q}$  is:

$$S(\vec{q}) = \frac{1}{N} \sum_{i,j} e^{i\vec{q} \cdot (\vec{r}_i - \vec{r}_j)} \langle \vec{S}_i \cdot \vec{S}_j \rangle. \quad (45)$$

We compute  $S(\vec{q})$  at key wavevectors:  $(\pi, \pi)$  (Néel ordering),  $(\pi, 0)$  and  $(0, \pi)$  (stripe ordering).

### B.7 Entanglement Entropy

For a bipartition into subsystems  $A$  and  $B$ , the von Neumann entropy is computed via singular value decomposition of the wavefunction reshaped as a matrix  $\psi_{i_A, i_B}$ :

$$S_A = - \sum_k \lambda_k^2 \log \lambda_k^2, \quad (46)$$

where  $\lambda_k$  are the singular values.

## C Computational Details and Reproducibility

### C.1 Software Stack

- Python 3.8+
- QuSpin 0.3.6+ for exact diagonalization
- PyTorch 1.9+ for Q-VAE implementation
- NumPy, SciPy for numerical operations
- scikit-learn for clustering and dimensionality reduction
- Pydantic for configuration validation
- HDF5 (h5py) for data storage

## C.2 Exact Diagonalization Details

The Hamiltonian is constructed in the  $S_{\text{tot}}^z = 0$  sector using QuSpin’s `spin_basis_general` with  $N_{\text{up}} = N/2$ . Ground states are computed using SciPy’s `eighs` (ARPACK Lanczos) with convergence tolerance  $10^{-10}$  and maximum 1000 iterations. The Hamiltonian is stored in CSR sparse format.

For  $L = 4$ :  $\dim(\mathcal{H}_{S^z=0}) = \binom{16}{8} = 12,870$

## C.3 Checkpointing and Resumption

The pipeline supports checkpointing at multiple stages:

- ED checkpoints: Ground states saved per lattice size after completion
- Q-VAE checkpoints: Model weights, training history, and best validation state
- Analysis checkpoints: Latent representations, observables, and intermediate results

All data is stored in HDF5 format with metadata for reproducibility.

## C.4 Parallel Execution

ED computations support parallel execution across parameter points using Python’s `multiprocessing.Pool`. Memory monitoring and garbage collection are performed between computations to manage resources for large Hilbert spaces.

## C.5 Validation Framework

The validation module performs automated checks:

- Néel phase validation: Requires  $|r(\text{latent}, m_s)| \geq 0.7$  for  $J_2/J_1 \in [0, 0.4]$
- Stripe phase validation: Requires  $|r(\text{latent}, m_{\text{stripe}})| \geq 0.7$  for  $J_2/J_1 \in [0.6, 1.0]$
- Literature comparison: Critical points compared against DMRG/QMC bounds

All code and data will be released under open licenses at <https://github.com/YCRG-Labs/prometheus-heisenberg-discovery>.

## D Complete Observable Data

Table 4 presents the complete set of computed observables for all 41 parameter points. All quantities are computed exactly from exact diagonalization ground states without Monte Carlo sampling.

## E Latent-Observable Correlation Matrix

Table 5 presents the complete Pearson correlation matrix between all eight latent dimensions and the physical observables with non-zero variance. Correlations with  $|r| \geq 0.7$  are highlighted.

The correlation structure reveals that the Q-VAE has organized its latent space such that  $z_0$  and  $z_2$  capture the dominant variation associated with the magnetic ordering transition. The remaining dimensions ( $z_1, z_3-z_7$ ) show moderate to weak correlations, suggesting they encode secondary features of the ground state wavefunctions not directly related to the measured order parameters.

Table 4: Complete observable data for  $L = 4$  across all parameter points. Energy density  $e$ , staggered magnetization  $m_s$ , plaquette order  $P$ , and structure factors  $S(\pi, \pi)$ ,  $S(\pi, 0)$  are shown. Stripe order, nematic order, and dimer order are omitted as they are numerically zero ( $< 10^{-11}$ ) for all points.

$J_2/J_1$	$e$	$m_s$	$P$	$S(\pi, \pi)$	$S(\pi, 0)$
0.30	-2.332	0.902	1.890	13.02	-0.185
0.31	-2.318	0.897	1.882	12.87	-0.179
0.32	-2.304	0.892	1.873	12.72	-0.172
0.33	-2.291	0.886	1.863	12.56	-0.164
0.34	-2.278	0.880	1.852	12.38	-0.155
0.35	-2.265	0.873	1.840	12.20	-0.145
0.36	-2.252	0.866	1.827	12.01	-0.133
0.37	-2.240	0.859	1.813	11.81	-0.120
0.38	-2.228	0.851	1.798	11.59	-0.105
0.39	-2.216	0.843	1.781	11.37	-0.088
0.40	-2.205	0.834	1.763	11.13	-0.068
0.41	-2.193	0.825	1.743	10.89	-0.045
0.42	-2.183	0.815	1.722	10.62	-0.019
0.43	-2.172	0.804	1.699	10.35	+0.011
0.44	-2.163	0.793	1.673	10.06	+0.046
0.45	-2.153	0.781	1.645	9.75	+0.086
0.46	-2.144	0.768	1.615	9.43	+0.134
0.47	-2.136	0.754	1.582	9.10	+0.189
0.48	-2.128	0.739	1.547	8.75	+0.254
0.49	-2.121	0.724	1.508	8.38	+0.331
0.50	-2.114	0.707	1.466	8.00	+0.421
0.51	-2.109	0.689	1.420	7.60	+0.527
0.52	-2.104	0.670	1.369	7.19	+0.652
0.53	-2.100	0.650	1.314	6.77	+0.800
0.54	-2.096	0.629	1.254	6.32	+0.976
0.55	-2.094	0.606	1.188	5.87	+1.185
0.56	-2.093	0.581	1.117	5.40	+1.431
0.57	-2.094	0.554	1.039	4.91	+1.721
0.58	-2.095	0.525	0.954	4.42	+2.061
0.59	-2.099	0.494	0.864	3.90	+2.454
0.60	-2.104	0.460	0.768	3.38	+2.901
0.61	-2.110	0.422	0.670	2.85	+3.399
0.62	-2.119	0.381	0.573	2.32	+3.937
0.63	-2.130	0.335	0.480	1.80	+4.497
0.64	-2.143	0.285	0.395	1.30	+5.058
0.65	-2.158	0.229	0.321	0.84	+5.596
0.66	-2.174	0.163	0.259	0.42	+6.093
0.67	-2.192	0.061	0.209	0.06	+6.538
0.68	-2.212	0.126	0.169	-0.25	+6.926
0.69	-2.233	0.180	0.138	-0.52	+7.258
0.70	-2.255	0.216	0.114	-0.74	+7.541

Table 5: Complete correlation matrix between latent dimensions and physical observables. Values with  $|r| \geq 0.7$  indicate strong correlations. Observables with zero variance (stripe order, nematic order, dimer order, entanglement entropy) are omitted.

Observable	$z_0$	$z_1$	$z_2$	$z_3$	$z_4$	$z_5$	$z_6$	$z_7$
Energy	<b>0.98</b>	0.55	<b>0.90</b>	-0.24	-0.60	-0.52	0.25	0.54
$m_s$	-0.97	-0.54	-0.90	0.22	0.59	0.49	-0.22	-0.53
$S(\pi, \pi)$	-0.97	-0.54	-0.90	0.22	0.59	0.49	-0.23	-0.53
$S(\pi, 0)$	<b>0.96</b>	0.53	<b>0.89</b>	-0.20	-0.58	-0.46	0.20	0.51
$S(0, \pi)$	<b>0.96</b>	0.53	<b>0.89</b>	-0.20	-0.58	-0.46	0.20	0.51
Plaquette	-0.97	-0.54	-0.90	0.22	0.59	0.48	-0.22	-0.52